Nano Energy 41 (2017) 101–108

Contents lists available at ScienceDirect

Nano Energy

journal homepage: www.elsevier.com/locate/nanoen

Full paper

Polarization-induced saw-tooth-like potential distribution in zincblende-wurtzite superlattice for efficient charge separation

Kai Zhang[a,1], Yawen Dai[a,c,1], Zhaohui Zhou[b], Saad Ullah Jan[a,c], Liejin Guo[b,*], Jian Ru Gong[a,*]

[a] CAS Key Laboratory for Nanosystem and Hierarchical Fabrication, National Center for Nanoscience and Technology, Beijing 100190, PR China
[b] International Research Center for Renewable Energy, State Key Laboratory of Multiphase Flow in Power Engineering, Xi'an Jiaotong University, Xi'an 710049, PR China
[c] University of Chinese Academy of Sciences, Beijing 100049, PR China

ARTICLE INFO

Keywords:
Polarization
Superlattice
Charge separation
Photocatalysis
Water splitting
Hydrogen production

ABSTRACT

Hydrogen production from solar water splitting over semiconductors shows great potential in solving the urgent energy and environmental issues, but its energy conversion efficiency is always restricted by the insufficient utilization of photogenerated charge carriers. Introducing built-in electric fields is a promising strategy for achieving efficient charge utilization in photocatalysts. However, the representative examples of built-in electric fields reported to date all have their own insurmountable shortcomings. Herein, we demonstrated that the zincblende-wurtzite (ZB-WZ) superlattice structure which widely spreads in II-VI and III-V group semiconductors is a promising candidate for the sufficient utilization of photogenerated charge carriers. We developed the ZB-WZ superlattice structures in a model semiconductor photocatalyst, $Cd_{1-x}Zn_xS$, by employing the oriented-attachment growth mechanism, and realized highly efficient photocatalytic hydrogen production under visible light irradiation with an excellent apparent quantum yield of 48.7% at 425 nm. Then the huge impact of the ZB-WZ superlattice structure on the photocatalytic performance was proved by the strong reciprocal relationships between the percentage of the nanocrystals with superlattice structures and the photoluminescence intensity, as well as that between the photoluminescence intensity and the photocatalytic activity. Moreover, theoretical simulation demonstrated that the spatial separation and alternate accumulation of electrons and holes around ZB/WZ interfaces is dominated by the polarization-induced saw-tooth potential distribution in the ZB-WZ superlattice rather than the staggered band alignment, and the intensities of built-in electric fields in adjacent ZB and WZ segments can be tuned by changing the specific configuration of the ZB-WZ superlattice. These findings open a new pathway for the development of novel and efficient semiconductor photocatalysts by tuning the superlattice structure with atomic precision, which will greatly benefit the solar water splitting area.

1. Introduction

Hydrogen production from solar driven water splitting over semiconductor photocatalysts has attracted great attention for its enormous potential to solve the urgent energy crisis and environmental pollution problems [1]. But the conversion efficiency of solar energy into chemical fuels remains comparatively low, due in large part to the underutilization of electrons and holes generated in semiconductor photocatalysts [2–4]. To ensure sufficient charge utilization, a photocatalyst should harmonically guarantee high efficiencies of the entire charge separation, migration and collection processes instead one of them. Although the fundamental requirements are pretty clear, the research progress in this area is quite limited, as there have not been any configurations that can fully meet all these criteria to date. Introducing built-in electric fields is one of the most effective strategies for realizing efficient charge utilization at the present stage [5,6], since the electric field causes photogenerated electrons and holes to move in opposite directions, leading to the spatial separation of reduction and oxidation half reactions. Nevertheless, the typical examples of built-in electric fields to achieving this goal, including those in Schottky junctions, heterojunctions, and polymorph junctions [6], are all interfacial electric fields that can only be active around the heterointerface, i.e., they have no beneficial effects on the utilization of electrons and holes generated in bulk phase. Thus, the collection of charge carriers generated deep inside the semiconductor crystals is very often difficult, as considerable amount of the photogenerated charge carriers recombine before they can migrate to the crystal surface. In addition, the above junctions suffer from severe interface problems which greatly restrict

* Corresponding authors.
E-mail addresses: lj-guo@mail.xjtu.edu.cn (L. Guo), gongjr@nanoctr.cn (J.R. Gong).
[1] K. Z. and Y. D. contributed equally to this work.

http://dx.doi.org/10.1016/j.nanoen.2017.09.021
Received 9 June 2015; Received in revised form 31 August 2017; Accepted 10 September 2017
Available online 12 September 2017

them from playing their full potentials for charge utilization. For instance, the abrupt composition change and large lattice mismatch at the heterointerface always cause the instability of interface and lead to the formation of interface defect states [7–9], both of which are detrimental to the transfer of charge carriers across the interfaces. Under this context, ferroelectrics, which possess a spontaneous polarization arisen from the displacement of the centers of the positive and negative charges in their unit cells, have attracted considerable attention in recent years [5]. Because these ferroelectrics materials are not merely perfect for avoiding the above interface problems, but also can, to some extent, promote the utilization of charge carriers in bulk phase. Yet, the performance of those ferroelectric materials is still far from satisfactory or even lower than conventional systems, owing to their notably large band gaps, intrinsically poor conductivities, as well as relatively confined carrier accumulation regions which only distribute on the polarized surfaces. Therefore, the construction of built-in electric fields for the sufficient utilization of photogenerated electrons and holes in the entire semiconductor crystals remains a pivotal challenge for highly efficient photocatalytic water splitting.

To remedy this situation, here we propose an innovative and promising superlattice structure to tentatively overcome the above problems. II-VI and III-V group semiconductors as known generally adopt either cubic zincblende (ZB) or hexagonal wurtzite (WZ) crystal structure in nature. The atomic stacking sequence of ZB structure along its close-packed [111] direction can be denoted as A-B-C-A-B-C, while the WZ structure employs a stacking sequence of A-B-A-B in the [0001] direction [10,11]. In most cases, the two crystal structures have approximate lattice constants in their close-packed planes. Hence, ZB-WZ superlattice, a special type of polymorph junction which is completely free from interface instability and defect formation problems, can be developed by bridging ZB and WZ segments along the [111–0001] orientation alternately (Fig. 1a) [12]. Meanwhile, owing to the staggered band alignment between ZB and WZ allotropes [13,14], the photogenerated electrons and holes in the ZB-WZ superlattice are spatially localized into ZB and WZ segments respectively (Fig. 1b) [15–18]. Moreover, spontaneous polarization exists along the [0001] crystal orientation of WZ structure, whereas ZB structure is highly symmetric and polarization-free, thus resulting in a saw-tooth potential profile in the ZB-WZ superlattice (Fig. 1c) [18–22], which will promote the spatial separation of electrons and holes as well as their alternate accumulation at ZB/WZ interfaces. Therefore, under the synergetic effect of the Type II band alignment and the spontaneous polarization induced saw-tooth potential profile, the photogenerated electrons and holes in the ZB-WZ superlattice will be naturally separated and alternately accumulated around ZB/WZ interfaces without substantial bulk recombination. Though the spatial charge localization usually leads to the deterioration of the charge transfer ability along [111–0001] direction of the ZB-WZ superlattice [23,24], the spatially separated electrons and holes are able to migrate in the close-packed (111) and (0001) planes without hindrance [25], and the dramatically reduced overlap of electron and hole wave functions also causes the extension of the carrier lifetime [15,16]. That is, highly efficient utilization of photogenerated electrons and holes can be expected in the ZB-WZ superlattice structure, because the electrons and holes that alternately accumulated around the ZB/WZ interfaces can readily migrate to the crystal surface along the direction perpendicular to [111–0001] orientation, and then be consumed in the reduction and oxidation reactions effectively. Furthermore, considering the excellent solar spectrum responses and suitable band positions of II-VI and III-V group semiconductors [26–36], it is evident that the ZB-WZ superlattice structure holds enormous potentials for the application in photocatalytic water splitting.

Despite the unique structural and electric features of the ZB-WZ superlattice, the performance for solar hydrogen production of the semiconductors having this configuration remains scarcely explored, as the controlling of nanocrystal structures at the atomic scale is still a daunting challenge in nanoscience and technology. Earlier this century, Banfield et al. discovered an oriented-attachment growth mechanism when they were investigating the coarsening of nanocrystals [37–39], and found that planar defects including twin boundaries and stacking faults were the inevitable products during the oriented-attachment growth process of ZnS nanocrystals. Though the precise control of the lattice stacking sequence was not achieved, these findings have opened an important opportunity for us to primarily explore the roles of the ZB-WZ superlattice structure during photocatalytic water splitting process. Hence, we developed the ZB-WZ superlattice structures in $Cd_{1-x}Zn_xS$ crystals via the oriented-attachment mechanism by solvothermally treating the nanocrystals obtained after an ultrasonic assistant precipitation procedure (Here $Cd_{1-x}Zn_xS$ as a typical II-VI group semiconductor is selected as the model photocatalyst because of its excellent solar spectrum response and suitable conduction band position for water reduction). Then we systemically investigated the interdependent relationship among the atomic-scale structure, the photoluminescence property, and the photocatalytic performance of the synthesized nanocrystals, and found that the gradual formation of the ZB-WZ superlattice structures caused a significant decrease in the photoluminescence intensity of these nanocrystals, and the reduced recombination of photogenerated electrons and holes resulted in much higher photocatalytic hydrogen production activity, implying that the highly efficient hydrogen production activity was closely associated with the existence of the ZB-WZ superlattice structures. Finally, in combination with the first principle calculation based on density functional theory (DFT), we further demonstrated that the spatial separation and alternate accumulation of electrons and holes at the ZB/WZ heterointerfaces, which was dominated by the spontaneous polarization induced saw-tooth-like potential profile in the ZB-WZ superlattice, should take the major responsibility for the excellent photocatalytic hydrogen production performance.

2. Results and discussion

The morphology change and the lattice structure evolution of the nanocrystals during the entire synthesis process were systemically investigated by recording the transmission electron microscopy (TEM) and HRTEM images of the nanocrystals at different reaction stages (Fig. 2). It is clear in Fig. 2a and b that the nanocrystals with size of 5–8 nm are formed under ultrasonic wave irradiation, and no planar defect can be seen in these nanocrystals. After solvothermal treatment for 1 h, the size of nanocrystals increases to 15–20 nm, and bright/dark contrast stripes emerge in individual nanocrystals (Fig. 2c and d), which is the characteristic feature of nanocrystals with stacking faults. Further increasing the solvothermal time to 3 h, the bright/dark contrast stripes arise in almost every nanocrystal, indicating the massive formation of stacking faults (Fig. 2e) [40]; meanwhile, the crystal size further increases to 50–80 nm, and amorphous layers with a thickness of 2–3 nm exist on the surface of the nanocrystals (Fig. 2f). Notably, the morphology of nanocrystals undergoes a dramatic change when the solvothermal time is no more than 3 h, accompanying with the simultaneous formation of stacking faults in these nanocrystals. Afterwards, the solvothermal time was prolonged to 6 and 12 h. From the TEM and HRTEM images (Fig. 2g-j), it can be seen that the bright/dark contrast stripes are well preserved, implying that the prolonged solvothermal treatment has no influence on the lattice structure of nanocrystals, while the only change is that the amorphous layer completely disappears, along with the formation of a well-developed crystal surface.

The growth process of the nanocrystals was carefully investigated. When the solvothermal time is no more than 3 h, the growth of the nanocrystals is indeed dominated by the oriented-attachment mechanism [41,42]. The evidences supporting this inference can be found in the TEM and HRTEM images. For example, the adjacent nanocrystals in Fig. S1a share a common crystal orientation, meeting the prerequisite for oriented-attachment; Fig. 2e and S1b show that a nanocrystal is

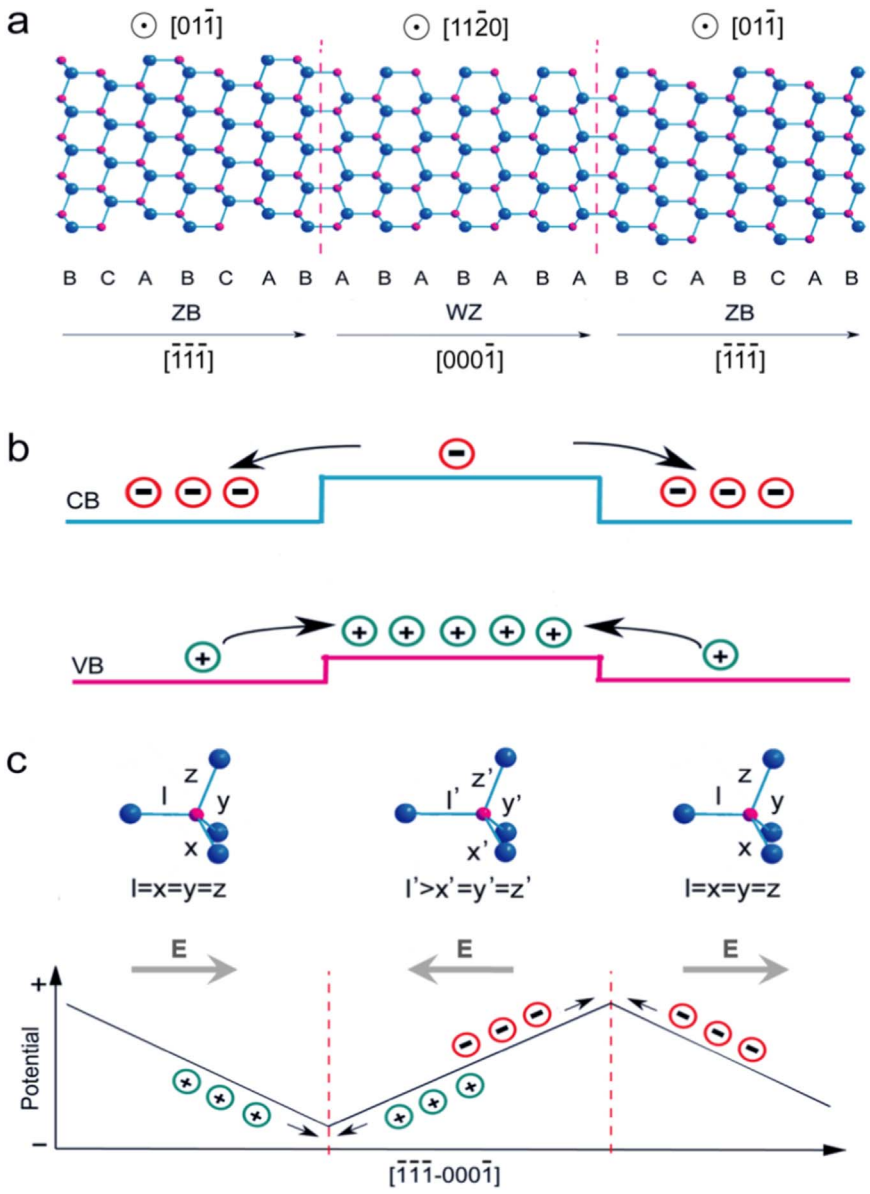

Fig. 1. (a) The atomic model for a ZB-WZ superlattice structure. The purple and blue balls represent cations and anions respectively. Each capital letter represents a cation-anion bilayer. The dot lines denote the stacking fault lines between different structures. (b) The typical staggered band alignment between ZB and WZ structures without consideration of spontaneous polarization. The corresponding charge transfer across their interface (Black arrows) is denoted. (c) The spontaneous polarization induced saw-tooth-like potential profile along the [111–0001] direction and the corresponding opposite built-in electric fields in adjacent ZB and WZ segments. The migration of charge carriers in different segments is shown, and tetrahedron units are drawn for ZB and WZ structures respectively to illustrate the difference in their detailed structures.

attached to another, accompanied with perfectly matching lattice fringes at the interface, which provides direct evidence for the oriented-attachment growth mechanism. In addition, the irregular and rough surface in Fig. S1c is also one of the characteristic features of nanocrystals grown via oriented-attachment mechanism. Hence, the formation of stacking faults was definitely the inevitable results of the oriented-attachment growth process [37–39]. As for the disappearance of amorphous layers at prolonged solvothermal time, it should be due to the occurrence of an Ostwald-ripening process [38].

To verify the formation of the ZB-WZ superlattice structure, we drilled down into the morphology and the lattice structure of the nanocrystals obtained after solvothermal treatment for 24 h. The XRD pattern in Fig. S2 shows distinctive diffraction peaks corresponding to the (111), (220), and (311) peaks of zincblende structure, which locate between the peaks of cubic CdS and ZnS, confirming the formation of $Cd_{1-x}Zn_xS$ solid solution with a major zincblende structure. And the (220) and (311) peaks are obviously broadened which could be related to the existence of stacking faults [43,44]. The scanning electron microscopy (SEM) image (Fig. 3a) shows that nanocrystals with sizes ranging from 50 to 150 nm spread over the entire micrograph, and most of them possess an irregular polyhedral morphology with ridges and valleys on their surfaces (See the inset), suggesting the presence of stacking faults [45,46]. Meanwhile, in the TEM image (Fig. 3b), the characteristic feature of stacking faults, i.e., the bright/dark contrast stripes, are ubiquitous [40]; repetitive stacking faults as well as occasionally arisen twin boundary can be easily found in Fig. 3c. To thoroughly explore the lattice structures of these nanocrystals, we analysed the zoomed-in HRTEM image and identified the atomic stacking sequence along the [0001] direction as denoted in Fig. 3d. Distinctly, the segments with stacking sequences of B-A-B-A and C-A-C-A belong to WZ structure, and the others are in ZB environment. Therefore, the co-existence of ZB and WZ segments in one nanocrystal is confirmed, implying that the ZB-WZ superlattice structure is successfully developed in metal sulphide nanocrystals via the oriented-attachment growth mechanism.

Given the successful synthesis of the desired model semiconductor nanocrystals, our next step is to explore the impact of the ZB-WZ superlatticle structures on the behaviour of photogenerated charge carriers. Hence, the photoluminescence spectra of the nanocrystals with different solvothermal time were recorded in Fig. 4a. With the increase of the solvothermal time, both the intensities of the near band edge emission peak located at ~ 620 nm and the defect state emission peak

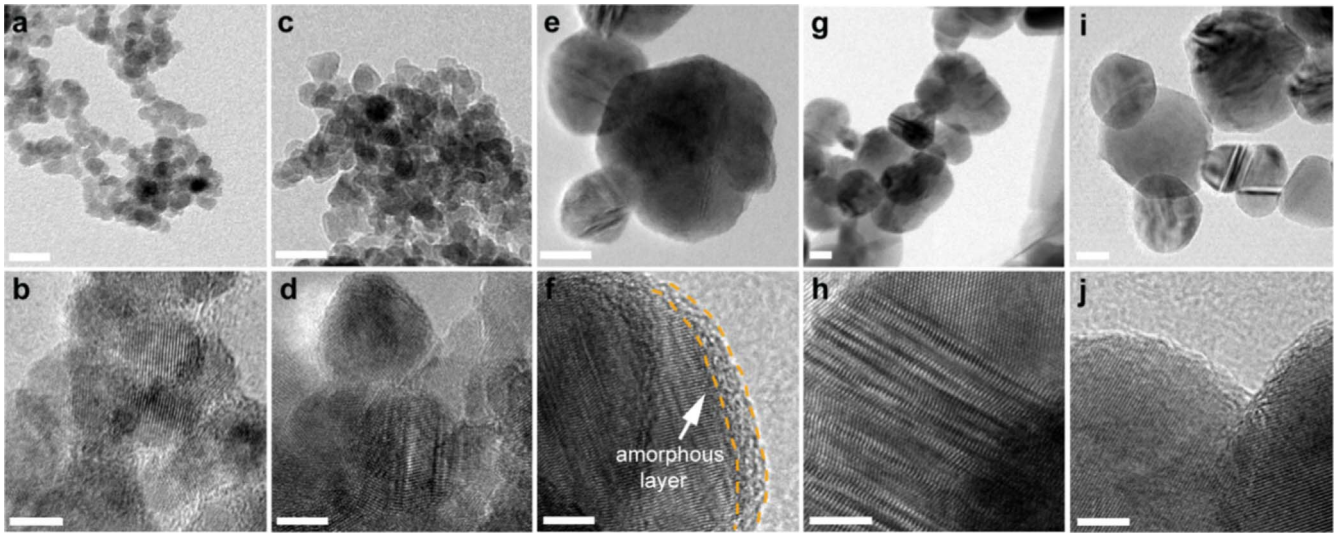

Fig. 2. TEM and the corresponding HRTEM images of the nanocrystals obtained at different reaction stages. (a) and (b), TEM and HRTEM images of the nanocrystals obtained after ultrasonic treatment; (c) - (j), TEM and HRTEM images of the nanocrystals obtained after solvothermal treatment for 1, 3, 6, and 12 h, respectively. Scale bars: 20 nm for all TEM images in the first row, 5 nm for all HRTEM images in the second row.

around ~ 690 nm rapidly decrease to only several percent of their initial levels. That is, the radiative recombination of the photogenerated electrons and holes is significantly reduced. To rule out the possible contribution of the difference in the light absorption ability and the external quenching effect of the surface absorbed groups for this decreased photoluminescence intensity, the synthesized nanocrystals were characterized by UV–Vis diffuse reflectance spectra and FT-IR spectroscopy respectively. The results in Fig. S3 and S4 clearly demonstrate that there is negligible difference in the light responses and the surface absorbed groups of the nanocrystals obtained at different reaction stages. Accordingly, the reduction in the radiative recombination should be the direct reflection of the enhanced charge separation efficiency of the synthesized nanocrystals. To further investigate the relationship between the improved charge separation ability and the emerged ZB-WZ superlattice structures, we counted the percentages of the nanocrystals with stacking faults in the synthesized samples, and correlated the variation of this percentage with the change in the photoluminescence intensity. It was found that the

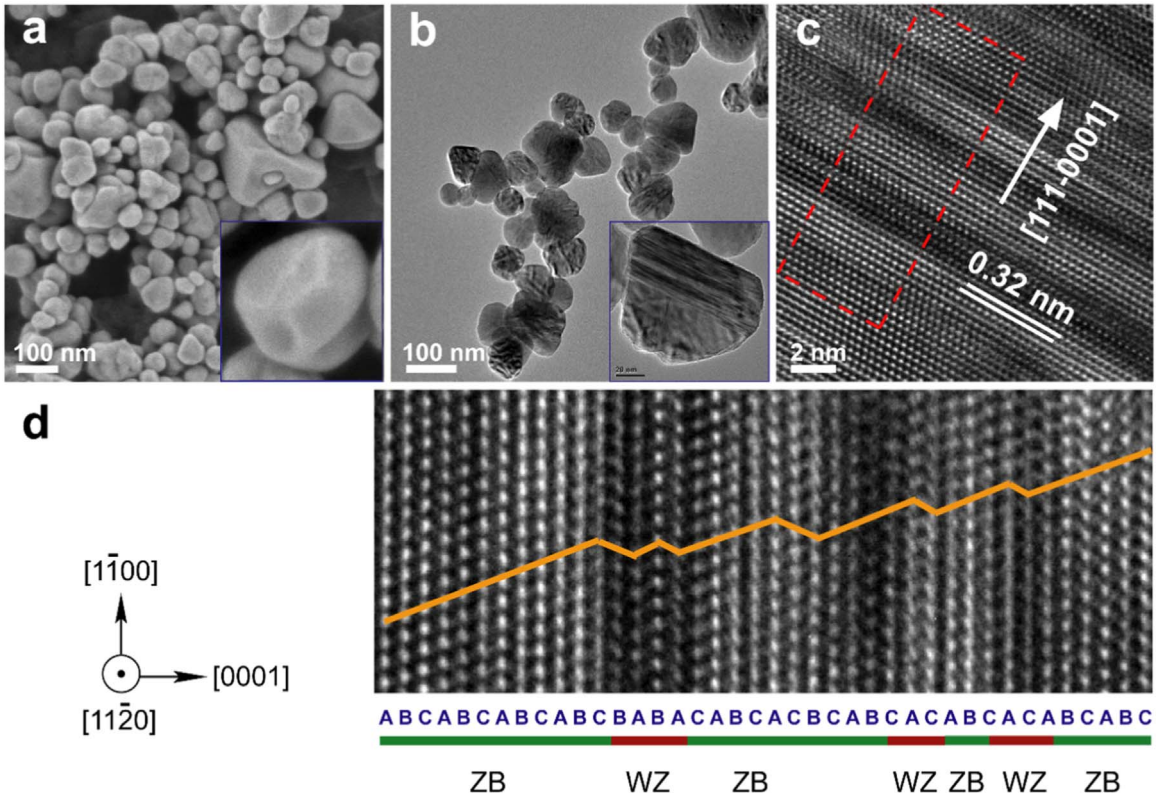

Fig. 3. (a) SEM, (b) TEM and (c) HRTEM images of the nanocrystals after solvothermal treatment for 24 h. The lattice distance of 0.32 nm is equivalent to the interplanar spacing of (111) planes in ZB structure or (0001) planes in WZ structure. (d) The zoomed-in image of the selected area in (c) with the atomic stacking sequence labelled by an orange folding line. The segments with different close-packed arrangements are identified.

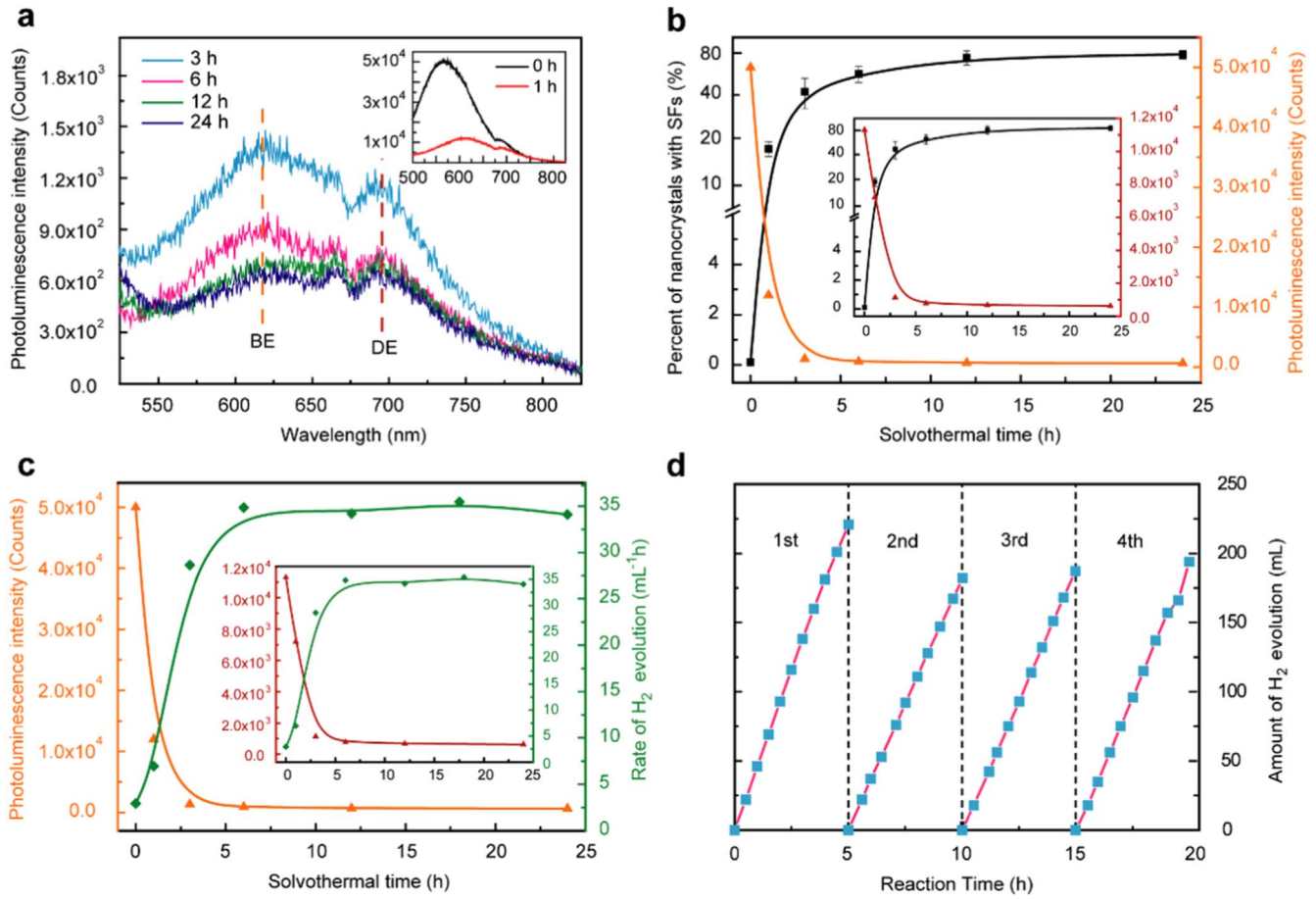

Fig. 4. (a) Photoluminescence spectra of the nanocrystals obtained at different reaction stages. (Excitation wavelength, 448 nm; BE, near band edge emission; DE, defect state emission.) (b) The antidependence of the photoluminescence intensity on the statistical percentage of the nanocrystals with stacking faults (SFs). (c) The inverse correlation between the photocatalytic hydrogen production activity and the photoluminescence property of the synthesized nanocrystals. (d) Long-term photocatalytic hydrogen production over the nanocrystals obtained after solvothermal treatment for 24 h.

photoluminescence intensity is antidependent on the percentage of the nanocrystals with stacking faults in the synthesized samples (Fig. 4b). Therefore, a preliminary conclusion that the formation of ZB-WZ superlatticle structures promotes the charge separation efficiency of the synthesized nanocrystals can be drawn from these results. Afterwards, we evaluated the photocatalytic hydrogen production properties under visible light irradiation of the synthesized nanocrystals. The variation of hydrogen production activity along with the increase of the solvothermal time is illustrated by the green curve in Fig. 4c. It is clear that the average hydrogen production rate increases rapidly when the solvothermal time is no more than 3 h, and then remains at a relatively stable level as the solvothermal treatment is longer than 6 h (Here the photocatalytic activity under visible light irradiation was originated from $Cd_{1-x}Zn_xS$ nanocrystals other than ZnS impurities as evidenced by the EDS mapping results in Fig. S5 and S6, and the impact of shape and size on the water splitting performance can be neglected according to the detailed analysis in Supplementary note 1). Then we compared the variation of photocatalytic activity with the change in the photoluminescence intensity and found a significant inverse correlation between them (Fig. 4c), implying that the separated photogenerated electrons and holes are efficiently utilized in photocatalytic water splitting reactions. We also calculated the exact value of hydrogen production rate and apparent quantum yield (AQY), and found that our $Cd_{1-x}Zn_xS$ nanocrystals with ZB-WZ superlattice structure outperform those purity-phase WZ or ZB $Cd_{1-x}Zn_xS$ nanocrystals reported in literatures [47–49]. The highest initial H_2 evolution rate is 44 mL h^{-1}, with an excellent AQY of 48.7% at 425 nm. This value is among the best results of the metal sulphide photocatalysts without using co-catalysts to date [36], and about 20% higher than that of the nanoparticles with twinning structures [50]. In addition, there is no significant decrease in the hydrogen production rate during the 4 cycles, displaying the excellent stability of the $Cd_{1-x}Zn_xS$ nanocrystals with the ZB-WZ superlattice structures.

To further prove the above conclusion, we performed the first principle calculation based on DFT by selecting CdS and ZnS as model materials (Fig. 5 and S4) [51]. Here, the macro-averaged electrostatic potential profiles as well as the plane averaged partial charge density distributions in the superlattice were both calculated by taking both the band alignment between ZB and WZ structures and the spontaneous polarization in WZ structure into consideration. Since the main findings in these theoretical simulations are quite similar by using either ZnS or CdS as the model material, analogous findings are supposed to be obtained in $Cd_{1-x}Zn_xS$ solid solution (see Fig. S7 and relate explanation for detailed analysis).

As shown in Fig. 5a, three typical $(3C)_m(2H)_n$ supercells including $(3C)_6(2H)_6$, $(3C)_6(2H)_{18}$, and $(3C)_{12}(2H)_{12}$ were built by bridging ZB and WZ CdS segments with different thicknesses repetitively. Here, $(3C)_6(2H)_6$ and $(3C)_{12}(2H)_{12}$ have the same thickness ratio of ZB to WZ segment (i.e., m/n) but different minimum repetitive periods (i.e., m + n), while $(3C)_6(2H)_{18}$ and $(3C)_{12}(2H)_{12}$ have the same minimum repetitive periods but different in the thickness ratios. So the simulation results can not only reveal the spatial distribution of charge carriers in the ZB-WZ superlattice structure, but will also shed some light on the relationship between the charge carrier distribution and the specific configuration of the ZB-WZ superlattice.

According to the calculated electrostatic potential profiles and the

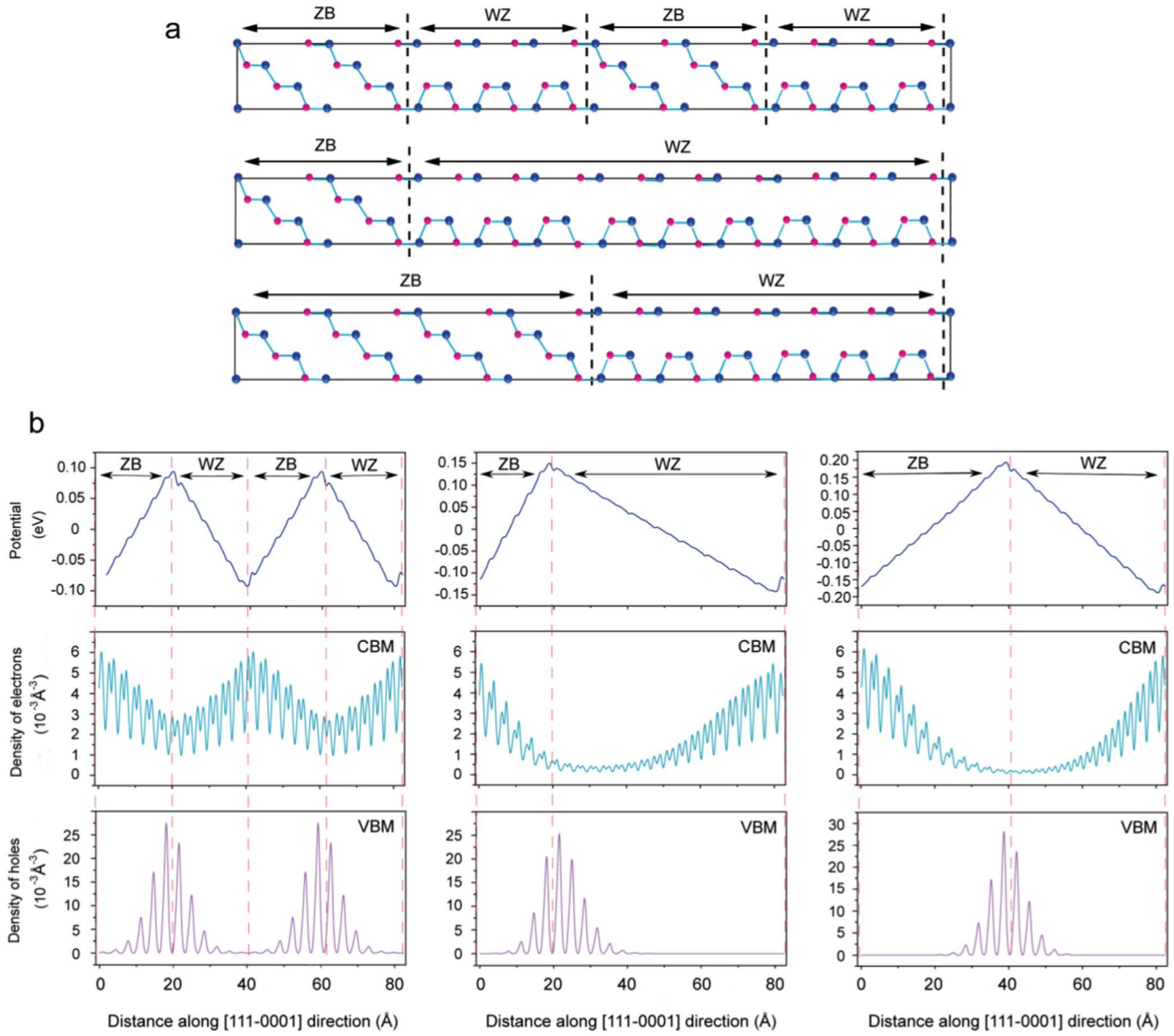

Fig. 5. (a) Structures of $(3C)_m(2H)_n$ CdS superlattice models for theoretical simulation and (b) the corresponding macro-averaged electrostatic potential profiles and plane averaged partial charge density distributions in CBM and VBM of the $(3C)_m(2H)_n$ superlattices.

partial charge density distributions in Fig. 5b, the saw-tooth-like potential profiles exist in all of these supercells [18,52–54], thus the electrons in the CBM and holes in the VBM are accumulated alternately around the ZB/WZ heterointerfaces, rather than being dragged into the inner part of the neighbouring ZB and WZ segments. Furthermore, the slopes of the electrostatic potential curves in the above three supercells are different from each other, meaning that both the change of the minimum repetitive period and the thickness ratio will cause the variation in the intensity of built-in electric field. Hence, we conclude that it is the spontaneous polarization induced saw-tooth-like potential distribution rather than the staggered band alignment that dominates the spatial separation and regional accumulation of charge carriers in the ZB-WZ superlattice, and the charge separation ability of the superlattice could be tuned by changing the specific configuration of the ZB-WZ superlattice [15–18,21,22]. This is rational, because the polarization in WZ structure are always neutralized by free charge at the surface of the crystal, hence free charges will locate at each interface between ZB and WZ segments in the ZB-WZ superlattice, leading to the formation of opposite built-in electric fields in the neighbouring ZB and WZ segments; once the configuration of the ZB-WZ superlattice varies, the polarization effect of WZ segment would be altered, thus changing the spatial accumulation of charge carriers around the ZB/WZ interfaces, finally leading to the fluctuation of the built-in electric field intensity [19–22]. Therefore, tuning the structure of the ZB-WZ superlattice at an atomic scale will be a promising strategy for the design of highly efficient II-VI or III-V group semiconductor photocatalysts in the future.

3. Conclusions

In summary, we elaborated the promising prospect of the ZB-WZ superlattice structure for the application in photocatalytic water splitting field and successfully developed such a superlattice structure in a typical II-VI group model semiconductor, $Cd_{1-x}Zn_xS$, via innovatively utilizing the oriented-attachment growth mechanism during the coarsening of nanocrystals. Afterwards, we found a negative correlation between the formation of the ZB-WZ superlattice structures and the photoluminescence intensity, and also observed that the variation of the photocatalytic hydrogen production activity is antidependent on the change of photoluminescence intensity, hence primarily proving

that the ZB-WZ superlattice structure is indeed promising for photocatalytic water splitting. Finally, with the aid of theoretical simulation, we demonstrated that the spatial separation and alternate accumulation of electrons and holes at the ZB/WZ heterointerfaces was dominated by the spontaneous polarization induced saw-tooth-like potential profile in the ZB-WZ superlattice rather than the staggered band alignment. Hence, we propose that tuning the structure of the ZB-WZ superlattice with atomic precision will be a promising strategy for developing highly efficient II-VI and III-V group semiconductor photocatalysts in the future [55–57]. These findings can contribute greatly to the solar water splitting area.

Acknowledgements

This work was financially supported by Natural Science Foundation of China (No. 51302046, 91123003, 51236007), Beijing Natural Science Foundation (No. 21422303), the Knowledge Innovation Program of the Chinese Academy of Sciences, and the China Postdoctoral Science Foundation (No. 2013M542343).

Appendix A. Supporting information

Supplementary data associated with this article can be found in the online version at http://dx.doi.org/10.1016/j.nanoen.2017.09.021.

References

[1] A. Fujishima, K. Honda, Electrochemical photolysis of water at a semiconductor electrode, Nature 238 (1972) 37–38.
[2] X. Chen, S. Shen, L. Guo, S.S. Mao, Semiconductor-based photocatalytic hydrogen generation, Chem. Rev. 110 (2010) 6503–6570.
[3] A. Kudo, Y. Miseki, Heterogeneous photocatalyst materials for water splitting, Chem. Soc. Rev. 38 (2009) 253–278.
[4] G. Xie, K. Zhang, B. Guo, Q. Liu, L. Fang, J.R. Gong, Graphene-based materials for hydrogen generation from light-driven water splitting, Adv. Mater. 25 (2013) 3820–3839.
[5] L. Li, P.A. Salvador, G.S. Rohrer, Photocatalysts with internal electric fields, Nanoscale 6 (2014) 24–42.
[6] H. Li, Y. Zhou, W. Tu, J. Ye, Z. Zou, State-of-the-art progress in diverse heterostructured photocatalysts toward promoting photocatalytic performance, Adv. Funct. Mater. 25 (2015) 998–1013.
[7] H.G. Kim, P.H. Borse, W. Choi, J.S. Lee, Photocatalytic nanodiodes for visible-light photocatalysis, Angew. Chem. 117 (2005) 4661–4665.
[8] J. Zhang, M. Zhang, R.Q. Sun, X. Wang, A facile band alignment of polymeric carbon nitride semiconductors to construct isotype heterojunctions, Angew. Chem. 124 (2012) 10292–10296.
[9] J.S. Jang, H.G. Kim, J.S. Lee, Heterojunction semiconductors: a strategy to develop efficient photocatalytic materials for visible light water splitting, Catal. Today 185 (2012) 270–277.
[10] J.E. Northrup, J. Ihm, M.L. Cohen, Electronic structure of zinc-blende-wurtzite interfaces: ZnS-ZnS (111-0001) and ZnSe-ZnSe (111-0001), Phys. Rev. B 22 (1980) 2060.
[11] C. Ricolleau, L. Audinet, M. Gandais, T. Gacoin, Structural transformations in II-VI semiconductor nanocrystals, Eur. Phys. J. D 9 (1999) 565–570.
[12] S. Takeuchi, K. Suzuki, Stacking fault energies of tetrahedrally coordinated crystals, Phys. Status Solidi A 171 (1999) 99–103.
[13] M. Murayama, T. Nakayama, Chemical trend of band offsets at wurtzite/zinc-blende heterocrystalline semiconductor interfaces, Phys. Rev. B 49 (1994) 4710.
[14] A. Belabbes, C. Panse, J. Furthmüller, F. Bechstedt, Electronic bands of III-V semiconductor polytypes and their alignment, Phys. Rev. B 86 (2012) 075208.
[15] K. Pemasiri, M. Montazeri, R. Gass, L.M. Smith, H.E. Jackson, J. Yarrison-Rice, S. Paiman, Q. Gao, H.H. Tan, C. Jagadish, Carrier dynamics and quantum confinement in type II ZB-WZ InP nanowire homostructures, Nano Lett. 9 (2009) 648–654.
[16] D. Spirkoska, J. Arbiol, A. Gustafsson, S. Conesa-Boj, F. Glas, I. Zardo, M. Heigoldt, M. Gass, A.L. Bleloch, S. Estrade, Structural and optical properties of high quality zinc-blende/wurtzite GaAs nanowire heterostructures, Phys. Rev. B 80 (2009) 245325.
[17] J.-M. Jancu, K. Gauthron, L. Largeau, G. Patriarche, J.-C. Harmand, P. Voisin, Type II heterostructures formed by zinc-blende inclusions in InP and GaAs wurtzite nanowires, Appl. Phys. Lett. 97 (2010) 041910.
[18] G. Jacopin, L. Rigutti, L. Largeau, F. Fortuna, F. Furtmayr, F. Julien, M. Eickhoff, M. Tchernycheva, Optical properties of wurtzite/zinc-blende heterostructures in GaN nanowires, J. Appl. Phys. 110 (2011) 064313.
[19] G.F. Neumark, Theory of the anomalous photovoltaic effect of ZnS, Phys. Rev. 125 (1962) 838.
[20] M. Miao, W.R. Lambrecht, Electronic structure of thin heterocrystalline superlattices in SiC and AlN, Phys. Rev. B 68 (2003) 155320.
[21] L. Li, L. Jin, J. Wang, D.J. Smith, W.J. Yin, Y. Yan, H. Sang, W.C. Choy, M.R. McCartney, Polarization-induced charge distribution at homogeneous zinc-blende/wurtzite heterostructural junctions in ZnSe nanobelts, Adv. Mater. 24 (2012) 1328–1332.
[22] L. Li, Z. Gan, M.R. McCartney, H. Liang, H. Yu, W.J. Yin, Y. Yan, Y. Gao, J. Wang, D.J. Smith, Determination of polarization-fields across polytype interfaces in InAs nanopillars, Adv. Mater. 26 (2014) 1052–1057.
[23] M. Schroer, J. Petta, Correlating the nanostructure and electronic properties of InAs nanowires, Nano Lett. 10 (2010) 1618–1622.
[24] C. Thelander, P. Caroff, S. Plissard, A.W. Dey, K.A. Dick, Effects of crystal phase mixing on the electrical properties of InAs nanowires, Nano Lett. 11 (2011) 2424–2429.
[25] N. Abdullayev, T. Kerimova, Influence of defects on charge and energy transfer in layered crystals, Phys. B: Condens. Matter 404 (2009) 5215–5217.
[26] D. Jing, L. Guo, A novel method for the preparation of a highly stable and active CdS photocatalyst with a special surface nanostructure, J. Phys. Chem. B 110 (2006) 11139–11145.
[27] C. Xing, Y. Zhang, W. Yan, L. Guo, Band structure-controlled solid solution of Cd1-xZnxS photocatalyst for hydrogen production by water splitting, Int. J. Hydrog. Energy 31 (2006) 2018–2024.
[28] K. Zhang, D. Jing, C. Xing, L. Guo, Significantly improved photocatalytic hydrogen production activity over Cd1-xZnxS photocatalysts prepared by a novel thermal sulfuration method, Int. J. Hydrog. Energy 32 (2007) 4685–4691.
[29] H. Yan, J. Yang, G. Ma, G. Wu, X. Zong, Z. Lei, J. Shi, C. Li, Visible-light-driven hydrogen production with extremely high quantum efficiency on Pt-PdS/CdS photocatalyst, J. Catal. 266 (2009) 165–168.
[30] M. Yoshida, A. Yamakata, K. Takanabe, J. Kubota, M. Osawa, K. Domen, ATR-SEIRAS investigation of the Fermi level of Pt cocatalyst on a GaN photocatalyst for hydrogen evolution under irradiation, J. Am. Chem. Soc. 131 (2009) 13218–13219.
[31] A. Yamakata, M. Yoshida, J. Kubota, M. Osawa, K. Domen, Potential-dependent recombination kinetics of photogenerated electrons in n-and p-type GaN photoelectrodes studied by time-resolved IR absorption spectroscopy, J. Am. Chem. Soc. 133 (2011) 11351–11357.
[32] J. Zhang, J. Yu, Y. Zhang, Q. Li, J.R. Gong, Visible light photocatalytic H_2-production activity of CuS/ZnS porous nanosheets based on photoinduced interfacial charge transfer, Nano Lett. 11 (2011) 4774–4779.
[33] Q. Li, B. Guo, J. Yu, J. Ran, B. Zhang, H. Yan, J.R. Gong, Highly efficient visible-light-driven photocatalytic hydrogen production of CdS-cluster-decorated graphene nanosheets, J. Am. Chem. Soc. 133 (2011) 10878–10884.
[34] M.G. Kibria, H.P. Nguyen, K. Cui, S. Zhao, D. Liu, H. Guo, M.L. Trudeau, S. Paradis, A.-R. Hakima, Z. Mi, One-step overall water splitting under visible light using multiband InGaN/GaN nanowire heterostructures, ACS Nano 7 (2013) 7886–7893.
[35] B. AlOtaibi, H. Nguyen, S. Zhao, M. Kibria, S. Fan, Z. Mi, Highly stable photoelectrochemical water splitting and hydrogen generation using a double-band InGaN/GaN core/shell nanowire photoanode, Nano Lett. 13 (2013) 4356–4361.
[36] K. Zhang, L. Guo, Metal sulphide semiconductors for photocatalytic hydrogen production, Catal. Sci. Technol. 3 (2013) 1672–1690.
[37] F. Huang, H. Zhang, J.F. Banfield, The role of oriented attachment crystal growth in hydrothermal coarsening of nanocrystalline ZnS, J. Phys. Chem. B 107 (2003) 10470–10475.
[38] F. Huang, H. Zhang, J.F. Banfield, Two-stage crystal-growth kinetics observed during hydrothermal coarsening of nanocrystalline ZnS, Nano Lett. 3 (2003) 373–378.
[39] F. Huang, J.F. Banfield, Size-dependent phase transformation kinetics in nanocrystalline ZnS, J. Am. Chem. Soc. 127 (2005) 4523–4529.
[40] B. Fultz, J.M. Howe, Transmission Electron Microscopy and Diffractometry of Materials, Springer Science & Business Media, 2012.
[41] J.F. Banfield, S.A. Welch, H. Zhang, T.T. Ebert, R.L. Penn, Aggregation-based crystal growth and microstructure development in natural iron oxyhydroxide biomineralization products, Science 289 (2000) 751–754.
[42] R.L. Penn, J.F. Banfield, Imperfect oriented attachment: dislocation generation in defect-free nanocrystals, Science 281 (1998) 969–971.
[43] V.V. Pujar, J.D. Cawley, Effect of stacking faults on the X-ray diffraction profiles of β-SiC powders, J. Am. Ceram. Soc. 78 (1995) 774–782.
[44] Z. Lu, J. Dahn, Effects of stacking fault defects on the X-ray diffraction patterns of T2, O2, and O6 structure $Li_{2/3}[Co_xNi_{1/3-x}Mn_{2/3}]O_2$, Chem. Mater. 13 (2001) 2078–2083.
[45] T. Xu, K.A. Dick, S. Plissard, T.H. Nguyen, Y. Makoudi, M. Berthe, J.-P. Nys, X. Wallart, B. Grandidier, P. Caroff, Faceting, composition and crystal phase evolution in III–V antimonide nanowire heterostructures revealed by combining microscopy techniques, Nanotechnology 23 (2012) 095702.
[46] M. Hjort, S. Lehmann, J. Knutsson, R. Timm, D. Jacobsson, E. Lundgren, K. Dick, A. Mikkelsen, Direct imaging of atomic scale structure and electronic properties of GaAs wurtzite and zinc blende nanowire surfaces, Nano Lett. 13 (2013) 4492–4498.
[47] D. Shu, H. Wang, Y. Wang, Y. Li, X. Liu, X. Chen, X. Peng, X. Wang, P. Ruterana, H. Wang, Composition dependent activity of $Fe_{1-x}Pt_x$ decorated ZnCdS nanocrystals for photocatalytic hydrogen evolution, Int. J. Hydrog. Energy (2016).
[48] Q. Li, H. Meng, J. Yu, W. Xiao, Y. Zheng, J. Wang, Enhanced photocatalytic hydrogen-production performance of graphene-$Zn_xCd_{1-x}S$ composites by using an organic S source, Chem. Eur. J. 20 (2014) 1176–1185.
[49] C.-C. Shen, Y.-N. Liu, X. Zhou, H.-L. Guo, Z.-W. Zhao, K. Liang, A.-W. Xu, Large improvement of visible-light photocatalytic H_2-evolution based on cocatalyst-free $Zn_{0.5}Cd_{0.5}S$ synthesized through a two-step process, Catal. Sci. Technol. 7 (2017) 961–967.
[50] M. Liu, L. Wang, G.M. Lu, X. Yao, L. Guo, Twins in $Cd_{1-x}Zn_xS$ solid solution: highly

efficient photocatalyst for hydrogen generation from water, Energy Environ. Sci. 4 (2011) 1372–1378.
[51] Z. Zhou, M. Li, P. Wu, L. Guo, Revisiting the zinc-blende/wurtzite heterocrystalline structure in CdS, Adv. Cond. Matter Phys. 2014 (2014).
[52] A. Qteish, V. Heine, R. Needs, Polarization, band lineups, and stability of SiC polytypes, Phys. Rev. B 45 (1992) 6534.
[53] M. Posternak, A. Baldereschi, A. Catellani, R. Resta, Ab initio study of the spontaneous polarization of pyroelectric BeO, Phys. Rev. Lett. 64 (1990) 1777.
[54] F. Bechstedt, P. Käckell, A. Zywietz, K. Karch, B. Adolph, K. Tenelsen, J. Furthmüller, Polytypism and properties of silicon carbide, Phys. Status Solidi B 202 (1997) 35–62.
[55] R. Algra, M. Verheijen, M. Borgstrom, L.-F. Feiner, G. Immink, W. van Enckevort, E. Vlieg, E. Bakkers, Twinning superlattices in indium phosphide nanowires, Nature 456 (2008) 369–372.
[56] P. Caroff, K.A. Dick, J. Johansson, M.E. Messing, K. Deppert, L. Samuelson, Controlled polytypic and twin-plane superlattices in III–V nanowires, Nat. Nanotechnol. 4 (2009) 50–55.
[57] K.A. Dick, C. Thelander, L. Samuelson, P. Caroff, Crystal phase engineering in single InAs nanowires, Nano Lett. 10 (2010) 3494–3499.